Non-Perturbative Probing Atomic Ionization by Attosecond Pulse Trains

Sebastián D. López *, Matías L. Ocello, Martín Barlari, Diego G. Arbó *

Posted Date: 15 April 2026

doi: 10.20944/preprints202604.1058.v1

Keywords: atomic photoionization; RABBIT; non-perturbative theory; attosecond chronoscopy; phase delays; attosecond pulse train

 doi:10.20944/preprints202604.1058.v1

Article

Non-Perturbative Probing Atomic Ionization by Attosecond Pulse Trains

Sebastián D. López [1,*], Matías L. Ocello [2,3], Martín Barlari [2,3] and Diego G. Arbó [2,3,4,*]

[1] Instituto de Investigaciones en Energía No Convencional - INENCO (UNSa - CONICET), Av. Bolivia 5150, 4400, Salta Capital, Argentina
[2] Institute for Astronomy and Space Physics - IAFE (UBA-CONICET), C1428GA, Buenos Aires, Argentina
[3] Universidad de Buenos Aires, Facultad de Ciencias Exactas y Naturales, Departamento de Física. C1428EGA Buenos Aires, Argentina
[4] Universidad de Buenos Aires, Ciclo Básico Común, Buenos Aires, Argentina
* Correspondence: sebastian.lopez@conicet.gov.ar (S.D.L.); diego@iafe.uba.ar (D.G.A.)

Abstract

We present a theoretical study focused on the photoelectron spectrum of near-infrared (NIR) laser-driven ionization of hydrogen atoms by attosecond pulse trains composed of several high-order harmonics of the former. We analyze the effects of increasing the intensity of the NIR probe laser to account for the interference of multiple quantum pathways arising from mainbands formed in ionization by the attosecond pulse train within the strong-field approximation (SFA) beyond the commonly used first-order perturbative (in the NIR laser intensity) reconstruction of attosecond beating by interference of two-photon transitions (RABBIT). The structure of the energy bands formed in the photoelectron spectrum is governed by quantum interferences of the photoelectron wave packet released within one optical cycle of the NIR probe laser field –intracycle interference– and by the number of active high harmonic components, leading to higher-order Fourier contributions as a function of the NIR–XUV relative phase delay. Our results demonstrate a significant departure from the standard two-path quantum-interference RABBIT picture, showing that both the phase-dependent oscillations of mainbands and sidebands and the extracted phase delays depend strongly on the probing laser intensity. The predictions of the SFA reveal that the above-threshold ionization bands exhibit systematic splitting and oscillation patterns as a function of the NIR intensity. SFA predictions are compared with results obtained within *ab initio* solutions of the time-dependent Schrödinger equation (TDSE), showing an excellent agreement, which evidences that the negligible effect of the Coulomb potential of the remaining ion on the escaping photoelectron for high energy above-threshold ionization. These findings provide new insights into attosecond chronoscopy in the strong-field regime.

Keywords: atomic photoionization; RABBIT; non-perturbative theory; attosecond chronoscopy; phase delays; attosecond pulse train

1. Introduction

The development of attosecond light sources and phase-controlled femtosecond laser pulses has enabled direct access to ultrafast electron dynamics in atoms and molecules [1–5]. The combination of extreme-ultraviolet (XUV) radiation with near-infrared (NIR) or visible laser fields in a pump-probe configuration constitutes the foundation of attosecond chronoscopy. The two main techniques developed are the attosecond streaking [6,7] and the reconstruction of attosecond beating by interference of two-photon transitions (RABBIT) [8,9].

In attosecond streaking, a single short isolated attosecond pulse ionizes the target and the released electron subsequently undergoes continuum–continuum transitions driven by the NIR probe field. In contrast, the RABBIT technique employs an attosecond pulse train (APT) field as the pump, composed of odd harmonics of a concomitant fundamental laser, which probes the XUV one-photon

 doi:10.20944/preprints202604.1058.v1

photoionization process. Both techniques allow one to infer temporal information associated with the dynamics of the electron wavepacket during the photoionization process. Moreover, the phase of the photoelectron during the photoionization can be retrieved indirectly by disentangling the phase accumulated by the electron wavepacket released during the continuum–continuum transitions by calculating the photoionization yield as a function of the relative phase between the APT and the probing laser field [10–14].

The standard theoretical description of RABBIT relies on a first-order perturbative treatment of the probe field, assuming absorption and emission of a single NIR photon after the absorption of consecutive odd XUV harmonics [11,15,16]. In this regime, perturbation theory comprising two-photon transitions (one XUV and one NIR) accurately describes the process and the observed interference pattern, which can be interpreted in terms of a two-path quantum-interference model [15,17–19]. However, as the probe field intensity escalates, higher-order multiphoton transitions in the continuum become relevant, and the assumption underlying the perturbative description progressively breaks down [20,21].

The process of single ionization of atoms by short laser pulses can be assessed by numerically solving the TDSE. Under certain conditions ($\beta_0 = U_P/2\omega c << 1$, where $U_P = (F_0/2\omega)^2$ is the ponderomotive energy of a free electron in a monochromatic laser of frequency ω), the dipole approximation can be regarded as valid and the solution of the TDSE is considered "exact" [22–24]. On the other hand, in addition to the computational costs of solving the TDSE, the underlying mechanisms that take place in the ionization process are hard to extract from the propagated wavepackets. To provide simple interpretations, several models have been developed depending on the parameters of the laser and emission energies. The most used models are those based on the SFA. To address these high-intensity probe fields, non-perturbative approaches based on the strong-field approximation (SFA) and semiclassical methods have proven to be particularly valuable [20,25–27]. By expressing the ionization amplitude as a coherent superposition of semiclassical trajectories associated with different ionization times, these approaches provide a simple physical interpretation of laser assisted photoionization, especially RABBIT processes [20,27–29]. In particular, semiclassical models naturally allow interpretations in terms of time-domain interferences, namely, intracycle and intercycle interferences [20,27]. Expressions for RABBIT signals accounting for ionization paths up to a specific order were recently derived [21] and a quantum path-integral model was developed to tailor attosecond time-resolved photoemission spectroscopy [30].

Fourth-order dipole transitions were considered to explain the oscillations in multi-sideband schemes for RABBIT [31,32]. Non-perturbative effects have been studied from a theoretical point of view in the strong field regime, where a multitude of quantum pathways contribute to the ionization process. These works have primarily focused on the case of an APT composed of only two odd harmonics, showing that the characteristic *checkerboard* structure in the energy-relative phase for above-threshold ionization (ATI) can be modified by increasing the probe intensity. In particular, the lowest-order two-path interference picture no longer applies when multiple continuum pathways become relevant. In a recent work, we showed how electron emission can be interpreted as a result of quantum interferences in the time domain for non-perturbative intensities of the NIR probing laser and found that phase delays depend strongly on the fundamental laser intensity [27]. In particular, in Ref. [27] we considered only two consecutive odd extreme ultraviolet (XUV) harmonics forming the APT to provide the simplest case.

In the present work, we study the relevant case of atomic photoionization by attosecond pulse trains (APT) composed of several successive odd harmonics assisted by a NIR probe laser treated by means of a strong-field non-perturbative description. We include several odd XUV harmonics to explore their influence on above-threshold ionization as the laser intensity increases. The inclusion of multiple XUV frequencies substantially increases the number of interfering quantum paths, leading to complex patterns in the final high harmonic mainbands (HH) and sidebands (SB) as a function of the relative phase between the APT pump and the NIR probe. We investigate how the interplay between

 doi:10.20944/preprints202604.1058.v1

the active number of harmonics, the probe field intensity, and the relative XUV–NIR phase shape the photoelectron spectra and their phase-dependent oscillations.

Using the strong-field approximation (SFA), we analyze the emergence of multi-path intracycle interference and perform a Fourier decomposition of the photoelectron spectrum (PES) to extract the lowest phase of non-trivial order, related to the Eisenbud-Wigner-Smith photoionization time delay. We compute higher-order Fourier components allowing for the characterization of the transition from the perturbative two-photon regime to a strongly non-perturbative multiphotonic interference regime. Comparisons with *ab initio* calculations of the time-dependent Schrödinger equation (TDSE) confirm the reliability of the SFA for energetic photoelectrons and provide physical insight into the mechanisms governing non-perturbative RABBIT interferometry.

The paper is organized as follows: In Sec. 2, we describe the non-perturbative theory based on the SFA used to evaluate the photoelectron spectra along the polarization direction in the RABBIT protocol. In Sec. 3, we present the results of the SFA and compare them to the *ab initio* calculations of the TDSE. Concluding remarks are presented in Sec. 4. Atomic units are used throughout the paper, unless otherwise stated.

2. Materials and Methods

We study the ionization by a linearly polarized attosecond pulse train consisting of a superposition of odd high-order harmonics (HH) with frequencies $(2m+1)\omega$, (where m is a positive integer number) accompanied by a near-infrared laser of frequency ω (NIR) [27]. In the length gauge of the dipole approximation, the laser pulse can be completely defined by its electric field

$$\vec{F}(t) = f(t)\left\{F_0\cos(\omega t+\phi)+\sum_m F_m\cos[(2m+1)\omega t+\phi_m]\right\}\hat{z}, \tag{1}$$

where $f(t)$ is the pulse envelope, F_0 corresponds to the field strength of the NIR component, ϕ its phase, and F_m and ϕ_m are the respective field strength and phases of the $(2m+1)$-th high-order harmonic component HH$(2m+1)$. In a region of a smooth envelope $f(t)$, the vector potential can be approximated as

$$\vec{A}(t) \simeq -\frac{f(t)}{\omega}F_0\sin(\omega t+\phi)\hat{z} \tag{2}$$

when $m \gg 1$ or the harmonic intensities are very small compared to the fundamental component. Here, we explore further limits of the RABBIT protocol for an attosecond pulse train of several HHs when the NIR probe intensity cannot be considered perturbative and the atomic potential can be neglected in the continuum.

The photoelectron emission spectrum can be calculated from the transition matrix T as

$$\frac{dP}{dE\sin\theta\, d\theta} = 2\pi\sqrt{2E}|T|^2, \tag{3}$$

where $E = \vec{k}^2/2$ is the electron emission energy, $\vec{k}$ the corresponding momentum, and θ the polar emission angle relative to the laser field polarization axis. Since we want to model regions where the energy of the emitted electron is far enough from the threshold, the effects of ionization by the NIR and core-electron interaction can be neglected. Within the SFA and the rotating wave approximation, the transition matrix T can be written as [20,23,27]

$$T = \sum_m T_m, \tag{4}$$

where each high-harmonic transition term can be calculated as

$$T_m = F_m\int_{-\infty}^{\infty}\ell(t)e^{i[S_m(t)-\phi_m]}dt, \tag{5}$$

 doi:10.20944/preprints202604.1058.v1

with

$$\ell(t) = -\frac{i}{2} f(t)\hat{z}\cdot\vec{d}\left[\vec{k}+\vec{A}(t)\right], \tag{6}$$

and the generalized Volkov phase is given by

$$S_m(t) = -\int_t^{\infty} dt' \left\{ \frac{\left[\vec{k}+\vec{A}(t')\right]^2}{2} + I_P - (2m+1)\omega \right\}. \tag{7}$$

In Eq. (6), $\vec{d}(\vec{v}) = \langle \vec{v}|\vec{r}|\varphi(r)\rangle$ is the dipole transition matrix element and I_P stands for the atomic ionization potential energy in Eq. (7).

If we consider the temporal translational symmetry for the vector potential, i.e., $\vec{A}(t+2\pi j/\omega) = \vec{A}(t)$, and for the generalized Volkov phase, i.e., $S_m(t+2\pi j/\omega) = S_m(t) + 2\pi a j/\omega$. We can factorize T_m in Eq. (5) as

$$T_m = F_m e^{-i\phi_m} \frac{\sin(a\pi N/\omega)}{\sin(a\pi/\omega)} e^{ia\pi(N-1)/\omega} I_m(\vec{k}), \tag{8}$$

where $a = \frac{k^2}{2} + I_P + U_P - (2m+1)\omega$ and

$$I_m(\vec{k}) = \int_0^{2\pi/\omega} \ell(t) e^{i[S_m(t)-\phi_m]} dt \tag{9}$$

corresponds to the intracycle amplitude factor, which is responsible for the phase modulation of the mainbands and sidebands as a function of ϕ and F_0. For a full proof of Eq. (8), the reader can see in Ref. [29]. The prefactors of Eq. (8) other than $I_m(\vec{k})$ correspond to the so-called intercycle amplitude factor, which gives rise to the formation of mainbands and sidebands for $a = 2n\pi$ (n integer) at energies

$$E_m^n = (2m+1+n)\omega - I_P - U_p. \tag{10}$$

To analyze the intracycle factor and its effects on the phase of the electron wavepacket in the SFA, we need to evaluate $I_m(\vec{k})$ in Eq. (9). For simplicity, we consider forward emission, i.e., $\vec{k} = k\hat{z}$. From here, the PES is analyzed at a particular mainband or sideband for even and odd n, respectively. When the APT is composed of a number ν of HHs in the range $\{m, m+1, ..., m+\nu-1\}$, the interferences in the PES [Eq. (3)] can be obtained spanning $|T|^2$ [see Eq. (4)] as

$$|T|^2 = \sum_j |T_j|^2 + 2\sum_{j<k} |T_j||T_k| \cos(\varphi_j - \varphi_k) \tag{11}$$

where $j,k \in \{m, m+1, ..., m+\nu-1\}$, and $\varphi_j = \arg[T_j]$. We want to mention that the phase delay contribution of each term in Eq. (11) is different. This fact leads to a complex behavior of the total phase delay for a particular mainband or sideband.

From Eq. (11), the inherent interference structure of HHs and SBs arises as a sum of several terms of different order. To get more insight into the behavior of the ATI peaks, we perform a Fourier analysis of the HHs and SBs signals as a function of ϕ as was done for the $\omega - 2\omega$ atomic photoionization in [25,26]. Therefore, the Fourier series decomposition will be performed as a function of F_0, for fixed HHs and SBs, i.e.,

$$P(F_0,\phi) = \frac{a_0(F_0)}{2} + \sum_{\mu=1}^{\infty} a_\mu(F_0)\cos(\mu\phi + \delta_\mu(F_0)), \tag{12}$$

where the coefficients $a_\mu(F_0)$ measure the amplitude of each term in the Fourier series and $\delta_\mu(F_0)$ is the phase delay of each term. Particularly, the Eisenbud-Wigner-Smith delay can be obtained for $\mu = 2$, i.e., $\delta_2(F_0)$ in the typical finite differences interpretation provided by RABBIT in the standard form for perturbative probe laser intensities, i.e., $A + B\cos(2\phi + \delta)$. We have shown in Appendix B of the paper [27] that in the strong field regime, phases φ_j are proportional to $n\phi$ and phase delays are integer fractions

 doi:10.20944/preprints202604.1058.v1

of π in all the cases, since SFA does not consider Coulombic electron-core interaction in the continuum. This demonstrates the full reliability of the Fourier analysis of the PES at mainbands and sidebands.

Considering that n is the number of energy steps of size ω to reach a particular mainband or sideband from the corresponding HH peak, we can observe for the particular case of a number ν of HHs, that the phase oscillations are given by harmonic combinations of $(n_j - n_k) = \pm 2, \pm 4, ..., \pm 2(\nu - 1)$ since the lowest energy difference between two neighboring HHs is 2ω, and between the lowest HH$(2m+1)$ and the highest HH$(2(m+\nu)-1)$ energy difference is $\pm 2(\nu-1)\omega$, as shown in Figure 1.

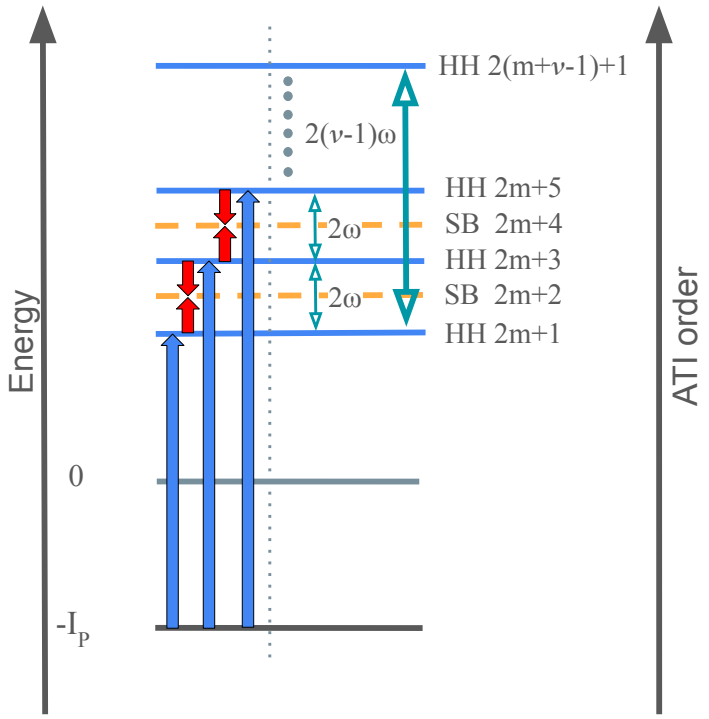

Figure 1. Scheme of transitions involved in the APT involving a number ν of high harmonics. Left: typical RABBIT protocol to reach a particular sideband. Right: minimum and maximum energy differences between high harmonics.

To clarify the previous analysis, we provide a couple of examples, one consisting of two HHs as was analyzed in Ref. [27] and another with three HHs. When the only two HHs considered are HH29 and HH31, i.e. $\nu = 2$, the difference $n_{29} - n_{31}$ is equal to ± 2 no matter which final mainband or sideband is analyzed. For example, to reach the sideband SB30, $n_{29} = 1$ and $n_{31} = -1$ leading to a $\cos(2\phi + \delta_2)$ interference term in Eq. (11), as expected. In the case of $\nu = 3$, for the HHs 27, 29, and 31, we have three interference terms in Eq. (11), two of them oscillate as $\cos(2\phi + \delta_{2,\alpha})$ with $\alpha = 1, 2$ for each of the two terms, since $n_{27} - n_{29} = n_{29} - n_{31} = \pm 2$ to reach any ATI band, whereas $n_{27} - n_{31} = \pm 4$ leads to $\cos(4\phi + \delta_4)$ for the remaining term. In the latter case, for sufficiently high laser intensities, the coherent sum in Eq. (11) triggers the exchange of three or more probe photons where the difference $(n_j - n_k) = \pm 4$. Transitions with energy differences greater than or equal to 2ω requires a larger laser field strength F_0 to observe the $\cos(4\phi + \delta_4)$ oscillation. In the next section we analyze these facts using the SFA theory to understand the photoelectron spectra as a function of F_0 and the phase ϕ. Finally, it is very important to recall that our theory considers a multitude of quantum paths (in fact, infinite paths), since it is not a perturbative treatment for the laser pulse as in the case of the typical RABBIT setup [15,17,18,33] where only two paths interfere as shown in the left side of Figure 1.

3. Results and Discussions

In the previous section, we have shown that the intracycle interference is the main responsible for the oscillations in the PES as we vary the phase ϕ [see Eqs. (8) and (9)]. We can retrieve the intracycle interference through the photoionization emission by an APT with a duration of only one cycle of the

 doi:10.20944/preprints202604.1058.v1

fundamental NIR laser, i.e., $\tau_X = 2\pi/\omega$ [27–29]. We show this case in Figure 2 for an APT composed of the three harmonics HH27, HH29, and HH31. For $\tau_X = 2\pi/\omega$ there is no formation of HHs or SBs due to the absence of intercycle interference. The intracycle interference exhibits a 2π periodic behavior as a function of the relative phase ϕ that follows the classical energy streaking of the photoelectrons with $F_0 = 0.003$, 0.005, and 0.008 in (a-b), (c-d), and (e-f), respectively. In dashed lines the classical streaking energy of photoelectrons ionized by the HH27, HH29, and HH31 without the probe field are displayed [see Eq.(A.1) in the Appendix A], showing a contact point between RABBIT and attosecond streaking techniques [30]. The interference structures become more complex as the probe laser intensity grows. It is worth mentioning the excellent agreement between the SFA results (left column) and the TDSE results (right column), which demonstrates the reliability of the SFA due to the negligible effect of the ionic core potential on the escaping photoelectron for the energy ranges in our study.

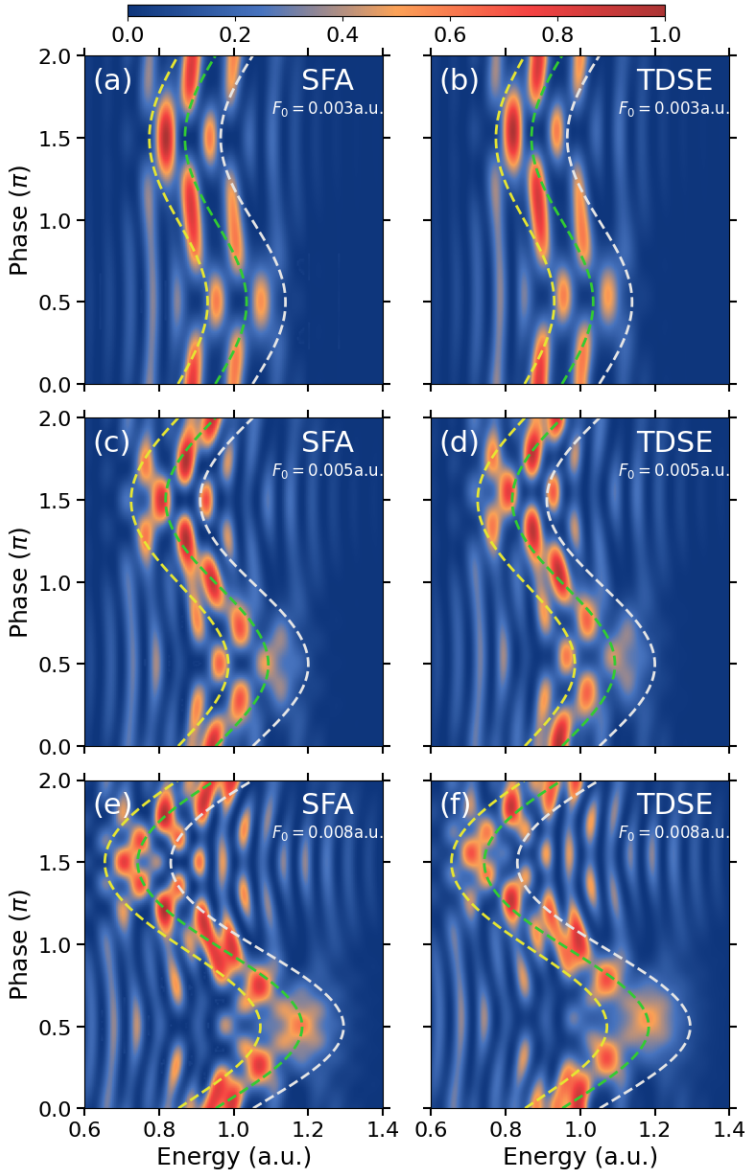

Figure 2. Photoelectron spectra for ionization of hydrogen in the forward direction as a function of the emission energy and the relative phase ϕ between the APT and the probing laser. The duration of the APT comprises one optical cycle of the probing laser ($\tau = 2\pi/\omega$). Photoelectron spectra are calculated for three XUV components HH27, HH29 and HH31. The SFA calculations are shown on the left column [(a), (c), and (e)], meanwhile TDSE calculations are shown in the right column [(b), (d), and (f)]. Calculations are performed for laser intensities $F_0 = 0.003$ a.u. in (a) and (b), $F_0 = 0.005$ a.u. in (c) and (d), and $F_0 = 0.008$ a.u. in (e) and (f). Dashed lines correspond to classical streaking energies of the three HHs [Eq. (A.1) in the Appendix A].

 doi:10.20944/preprints202604.1058.v1

For the case of a longer APT, HHs and SBs arise as a consequence of the intercycle interference among the electron wavepackets released at different NIR optical cycles [see the intercycle factor of Eq. (8)]. In Figure 3, we show calculations for APT with a duration of three optical cycles of the probe NIR laser, i.e., $\tau_X = 6\pi/\omega$ for the same intensity values as in Fig. 2. In this case, the intercycle interference allows for emission mainly in the mainbands (HHs, denoted by vertical dashed lines) and SBs according to Eq. (10). Whereas the intracycle interference pattern in Fig. 2 displays a 2π periodicity as a function of ϕ, the total (intra- and intercycle) ionization spectrograms in Fig. 3 are π-periodic. The horizontal bars show the classical energy ranges for each HH [see Eq.(A.2)] and give a rough idea of the range of the effect of each HH on neighboring ATI bands. In Fig. 3a and b we observe a typical two-lobe interference pattern as a function of ϕ since the probe laser intensity ($F_0 = 0.003$ a.u.) allows the exchange of only one probe photon, which is compatible with the first-order perturbative RABBIT theory. In other words, only two classical energy ranges overlap on SB28 and SB30 allowing for emission and absorption of only one ω photon. Whereas SBs peak at $\phi = 0$ and π, HHs do it at $\phi = \pi/2$ and $3\pi/2$, giving rise to phase delays $\delta_{SB} = 0$ and $\delta_{HH} = \pi$, respectively [see Eq. (12) with $\mu = 2$]. As the probe laser intensity grows, the number of visible marginal sidebands with energies higher than E^0_{15} (HH31) and lower than E^0_{13} (HH27) increases. More importantly, as the probe laser becomes more intense, the total interference pattern in the mainband and sidebands in Figure 3 present a higher number of lobes. For $F_0 = 0.005$ a.u. in Figure3 (c) and (d), the HH29 peak is affected by exchange of two probe photons after ionization produced by HH27 and HH31. In fact, all HHs and the SBs between HH27 and HH29 are affected by the exchange of two probe photons from all HHs. Nonetheless, the number of lobes in the marginal sidebands in Fig. 3 (c) and (d) is two, since not all the harmonics are affecting them. For example, HH31 does not affect the low-energy marginal sidebands, nor does HH27 affect the high-energy marginal sidebands, as their effective ranges do not cover them (horizontal bars). We observe a splitting of the lobes going from two lobes in Fig. 3(a) and (b) to four lobes in Figure 3 (c) and (d). It is clear that the influence of the (classically) allowed energies (shown in the Figure as horizontal bars) for each HH, is directly related to the increasing of the number of lobes. However, this number in HHs and sidebands does not increase from (d) to (e), despite the increase of the intensity of the probe laser. This stems from the fact that the number of HHs is $\nu = 3$ and the energy gap between the highest HH31 and the lowest HH27 in the APT is $2(\nu - 1)\omega = 4\omega$.

We explore the increase of the number of HH components accompanied by a high-intense NIR probe to observe the contributions to the many oscillations of the ATI bands. In Figure 4, we extend the above results for the case of four, five, and six HHs, plotting SFA results as a function of the electron emission energy and the relative phase ϕ between the APT and the probe laser for four ($\nu = 4$), five ($\nu = 5$), and six ($\nu = 6$) HH components in the panels (a), (b), and (c), respectively. In the cases where the probe laser intensity allows the overlap of classical energy ranges for the paths starting from all the HHs involved, we observe the interference modulations as $\cos[2(\nu - 1)\phi + \delta]$. For example, HH33 in Figure 4 (a) with six lobes and nodes, SB32 with eight lobes and nodes in Figure 4 (b), and SB32 in Figure 4 (c) with ten lobes and nodes. It is important to state that the interplay of different orders varies at different ATI peaks, making the visual inspection a very fuzzy tool for assessing its importance.

In order to show the above mentioned behaviors, we explore the effect of the laser intensity and the phase of each ATI band. In Figure 5, we show the effect of the probe laser intensity on the interference patterns of HH29, SB30, and HH31 as a function of the relative phase ϕ for the case of an APT formed with four HHs –from HH27 to HH33. We note that the structure of HHs and SBs becomes more complex as F_0 increases. For very low intensities, HH29 in Figure 5a and HH31 in Figure 5c have noticeable emission probabilities, with phases peaking at $\phi = \pi/2$ and $3\pi/2$. On the other hand, for SB30, the emission probability rises from zero at $F_0 = 0$, as expected, since this sideband can be reached only by absorbing NIR photons, and the probability distributions peak at $\phi = 0$ and $\phi = \pi$. These behaviors at low intensities were described in detail in Ref. [27]. As intensity increases (3×10^{-3} a.u. $\lesssim F_0 \lesssim 7 \times 10^{-3}$ a.u.), the lobe structures split to give rise to four lobes. For $F_0 \gtrsim 0.007$ a.u., a new splitting of the lobes gives rise to a total number of six lobes, reaching its maximum $2(\nu - 1)$ for $\nu = 4$ HHs.

 doi:10.20944/preprints202604.1058.v1

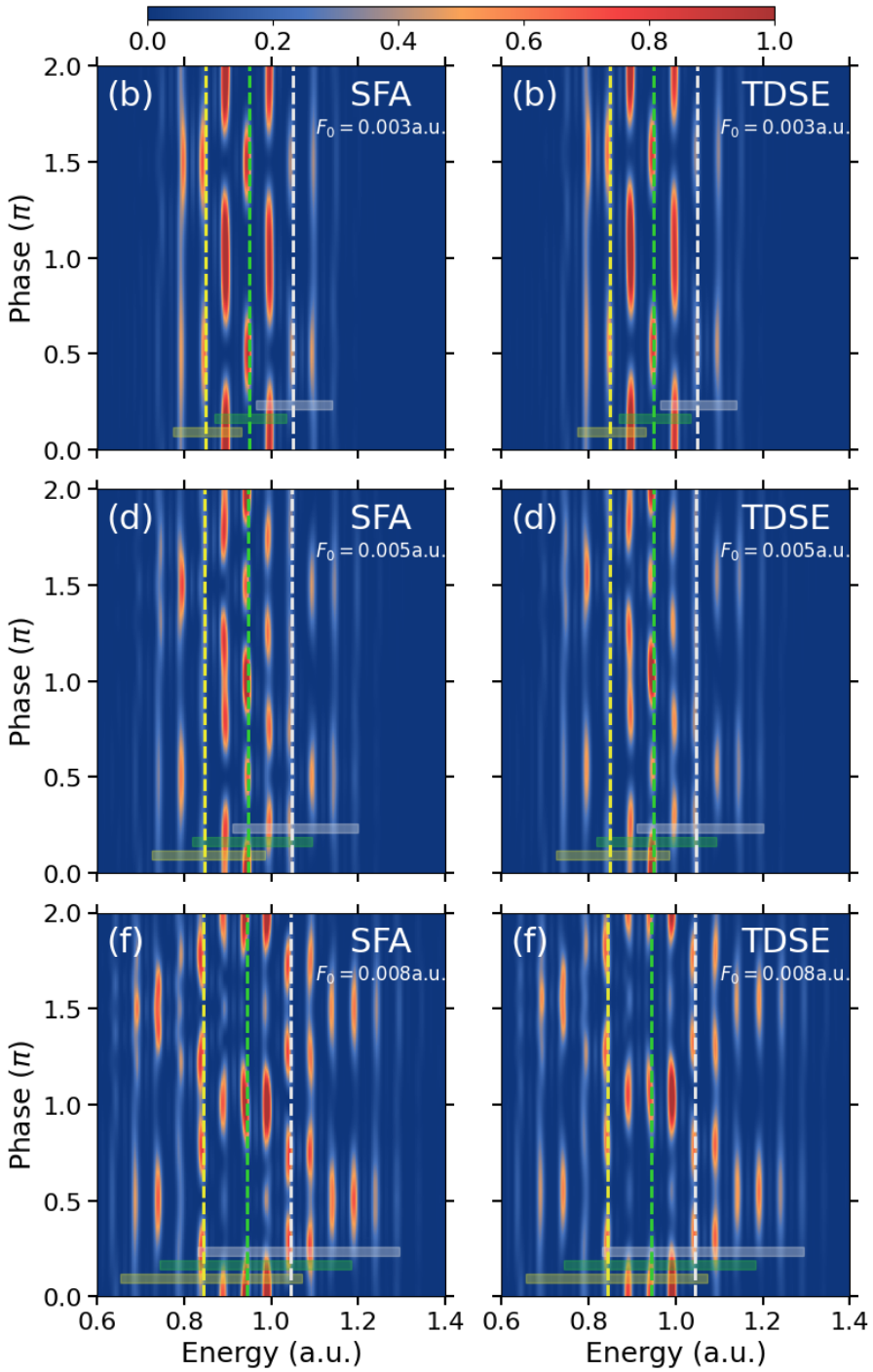

Figure 3. Photoelectron spectra for ionization of hydrogen in the forward direction as a function of the emission energy and the relative phase ϕ between the APT and the probing laser. The duration of the APT comprises three optical cycles of the probing laser ($\tau = 6\pi/\omega$). Photoelectron spectra are calculated for three XUV components HH27, HH29 and HH31. The SFA calculations are shown on the left column [(a), (c), and (e)], meanwhile TDSE calculations are shown in the right column [(b), (d), and (f)]. Calculations are performed for laser intensities $F_0 = 0.003$ a.u. in (a) and (b), $F_0 = 0.005$ a.u. in (c) and (d), and $F_0 = 0.008$ a.u. in (e) and (f). The peak positions of harmonics are shown with colored dashed vertical lines: HH27 (yellow), HH29 (green), HH31 (white). Light colored horizontal bars represent the classical energy ranges of each HH according to Eq. (A.2) in the Appendix A. Each bar is colored as its corresponding HH peak.

 doi:10.20944/preprints202604.1058.v1

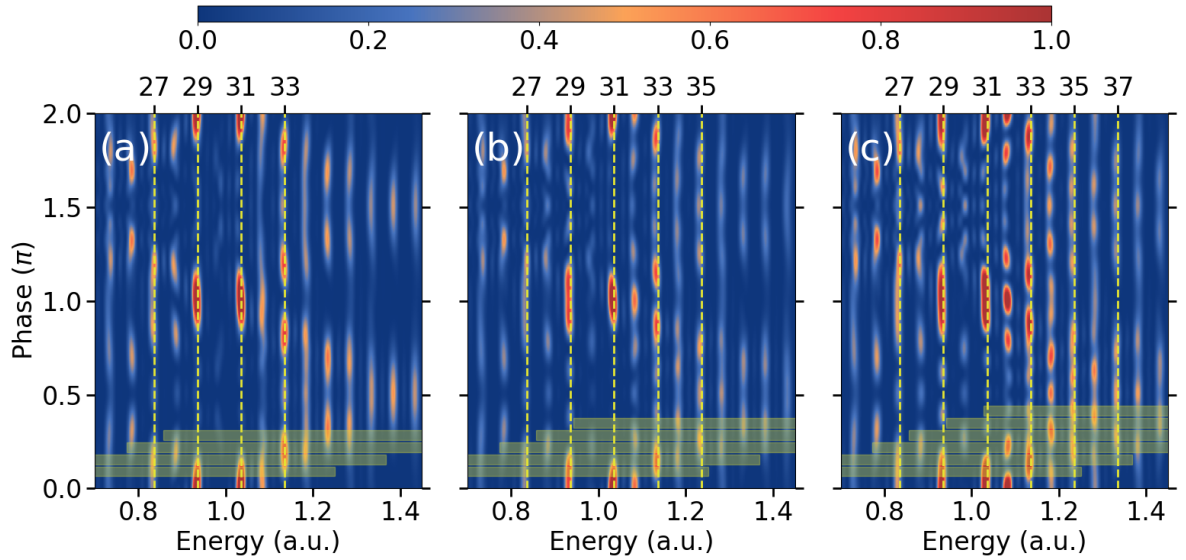

Figure 4. Photoelectron spectra for ionization of hydrogen in the forward direction as a function of the emission energy and the relative phase ϕ between the APT and the probing laser. In all the cases $F_0 = 0.012$ a.u. and the APT has duration of three optical cycles composed by the odd harmonics of order (a) HH27 to HH33, (b) HH27 to HH35, and (c) HH27 to HH37. The XUV field strengths is $F_X = 0.01$ a.u.. Light colored horizontal bars represent the classical energy ranges of each HH according to Eq. (A.2) in the Appendix A. Each bar is colored as its corresponding HH peak.

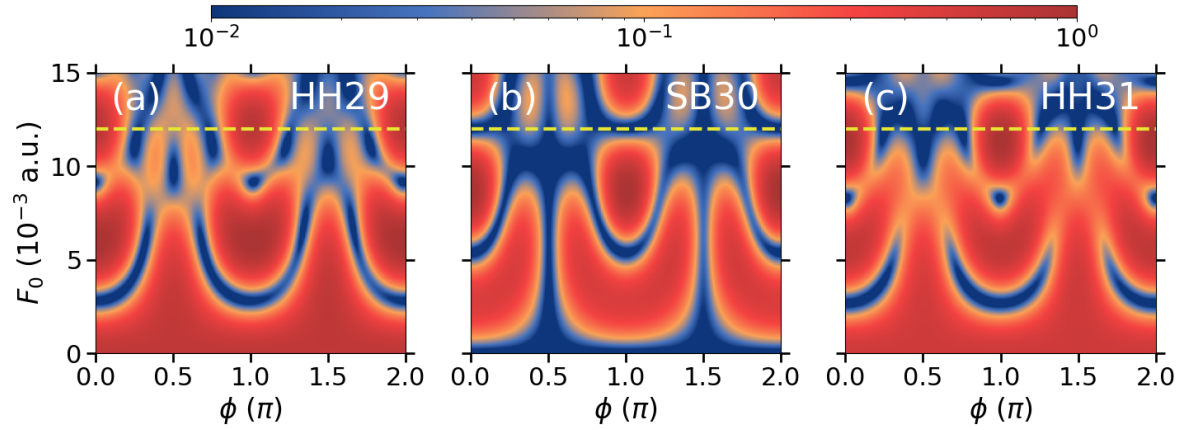

Figure 5. Photoelectron spectrum of forward emission as a function of the field strength F_0 and the relative phase ϕ in log scale for three different ATI bands: (a) HH29, (b) SB30, and (c) HH31. The APT is composed of four high-order harmonic components from HH27 to HH33. The yellow dashed line correspond to $F_0 = 0.012$ a.u. used in Figure 4 (a).

In Figure 6 we show the first even orders $\{0, 2, 4, 6, 8\}$ of the Fourier decomposition [Eq. 12] for the same three particular ATI peaks of the calculations shown in Figure 5, namely, HH29, SB30, and HH31 as a function of the increasing probe laser intensity. Odd orders are not shown since they are close to zero within the numerical error, as expected. We observe that Fourier components turn on gradually as the electric field increases for the first even orders. We can see that the last relevant order for this configuration is the 6th one [$2(\nu - 1)$ for the $\nu = 4$ components considered in the APT]. Naturally, this method does not allow to discriminate each interference term in Eq. (11), but it provides a simple way to extract the lowest phase delays related to the Wigner phase delay and phase delays of higher orders. On the other hand, the DC component $a_0(F_0)$ is different from zero for HHs at very low intensities, whereas for the SBs, the DC term is zero for $F_0 = 0$, as mentioned before.

 doi:10.20944/preprints202604.1058.v1

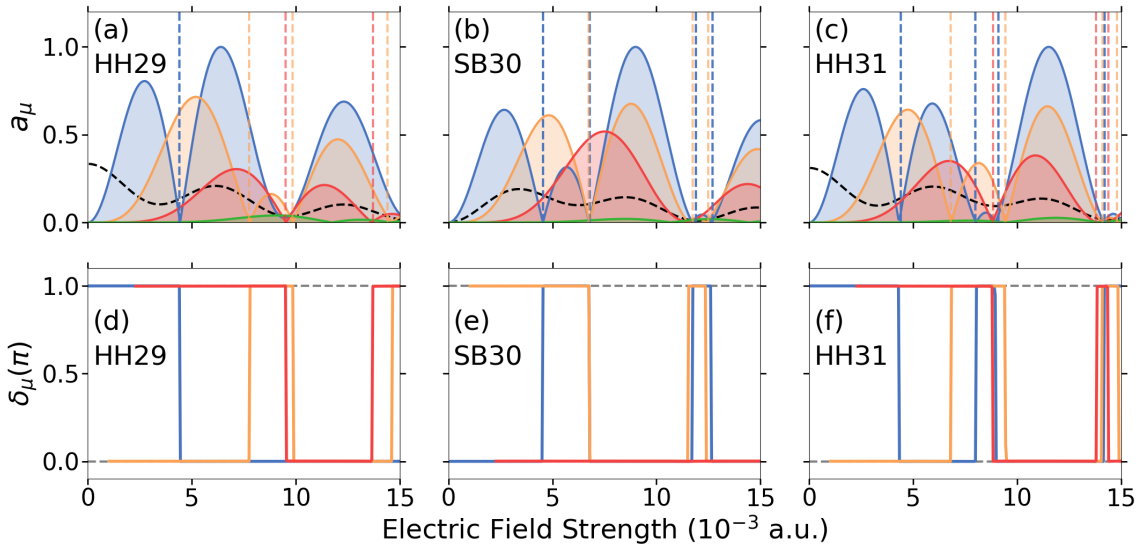

Figure 6. Even coefficients of Fourier decomposition in Eq. (12) of the photoelectron spectrum as a function of the intensity for (a) HH29, (b) SB30 and (c) HH31, and their respective phase delays in panels (d) to (f). Results for $\mu = \{0, 2, 4, 6, 8\}$ are displayed with colors black, blue, orange, red, and green, respectively. In the lower row we only show relevant phase delays corresponding to $\mu = \{2, 4, 6\}$. The APT is composed of HH_{27}, HH_{29}, HH_{31}, and HH_{33}.

In the lower row of Figure 6, we show the phase delays δ_μ as a function of the field strength. For perturbative intensities, where the term $\mu = 2$ dominates, $\delta_2 = 0$ for SBs and $\delta_2 = \pi$ for HHs, as expected in the typical perturbative RABBIT setup where the Coulomb interaction in the final channel is neglected [27,34]. As the field strength increases, δ_2 presents discrete jumps of π at particular values of F_0 where the coefficients $a_\mu(F_0)$ become null, as observed when comparing to the coefficients $a_\mu(F_0)$ in the first row of Figure 6. These values of F_0 are denoted as vertical dashed lines in Figure 6 with the corresponding colors to guide the eye. We observe an analogous behavior for the phases of higher orders, i.e., δ_4 and δ_6.

4. Conclusions

We have analyzed the photoelectron spectrum in the RABBIT setup using the SFA non-perturbatively, including all infinite quantum paths. We have scrutinized the structure of HHs and SBs with increasing intensity of the probe laser beyond the first-order perturbative limit when multiple harmonics are present in the APT. Due to intracycle interference, the presence of many HHs leads to a splitting of the number of oscillating structures (lobes) of HHs and SBs as a function of the relative phase ϕ as the intensity of the probe laser grows. We have demonstrated that the number of lobes as a function of ϕ is related to the number of active HHs affecting the mainband or SB under study, that is, the number of HHs whose energy ranges cover the studied HH or SB energy. We have also shown that the complexity of ATI structures increases with the number ν of HHs that form the APT. In this sense, we have performed a Fourier analysis to extract the Wigner (first-order) and higher-order phase delays. We have verified that the highest relevant order of HH or SB oscillations is $2(\nu - 1)$ at sufficient intensity of the probe laser. We have found that the phase delays of HHs and SBs experience discrete jumps of π for values of the intensity of the probe laser, corresponding to the zeros of their corresponding Fourier amplitudes. This jump implies a phase shift of $\pi/2$ in the phase ϕ between the fundamental and its harmonics breaking down the typical checkerboard arrangement of photoelectron spectra as a function of ϕ found in the first-order perturbative RABBIT setup. The TDSE results demonstrate that our study of the structures of the PES is valid for high emission energies because the SFA neglects the Coulomb interaction of the electron with the remaining core. Therefore, with the inclusion of quantum paths involving the exchange of more than two (XUV and NIR) photons, our results within the SFA could explain experimental measurements of time delays

 doi:10.20944/preprints202604.1058.v1

in photoionization processes, unlike the first-order perturbative RABBIT theory. Non-perturbative studies of angle-resolved emission within the SFA and on conditions with appreciable effects of the Coulomb potential of the parent ion on the photoelectron are highly needed by the community.

Author Contributions: Conceptualization, D.G.A. and S.D.L.; methodology, M.L.O., S.D.L., and D.G.A.; software, M.L.O., M.B., S.D.L, and D.G.A.; validation, M.L.O., S.D.L., and D.G.A.; formal analysis, M.L.O. and D.G.A.; investigation, M.L.O., S.D.L., and D.G.A.; resources, S.D.L. and D.G.A.; data curation, M.L.O., M.B., and S.D.L.; writing—original draft preparation, D.G.A. and S.D.L.; writing—review and editing, M.L.O., S.D.L., and D.G.A.; visualization, M.L.O.; supervision, S.D.L and D.G.A.; project administration, S.D.L and D.G.A.; funding acquisition, S.D.L and D.G.A. All authors have read and agreed to the published version of the manuscript.

Funding: This research was funded by Agencia I+D+i (Argentina) grant numbers PICT 2020-01755 and 2020-01434 and Consejo Nacional de Investigaciones Científicas y Técnicas (CONICET) (Argentina) grant number PIP 2022-2024 11220210100468CO. Programa Nacional RAICES Federal: Edición 2022 of Ministerio de Ciencia, Tecnología e Innovación (MinCyT), PICT 2023 RAÍCES FEDERAL 01-PICT-2023-02-10 from Agencia I+D+i (Argentina) and grant number PIP Raices 2023-2025 29320230100003CO of CONICET (Argentina).

Data Availability Statement: Data are contained in this article and can be solicited to the corresponding authors.

Acknowledgments: This work is supported by PICT 2020-01755 and 2020-01434 of ANPCyT (Argentina), PIP 2022-2024 11220210100468CO of Consejo Nacional de Investigaciones Científicas y Técnicas (CONICET) (Argentina) and Programa Nacional RAICES Federal: Edición 2022 of Ministerio de Ciencia, Tecnología e Innovación (MinCyT); PICT 2023 RAÍCES FEDERAL 01-PICT-2023-02-10 from Agencia I+D+i (Argentina); and PIP Raices 2023–2025 (grant number:29320230100003CO) of CONICET (Argentina).

Conflicts of Interest: The authors declare no conflicts of interest.

Abbreviations

The following abbreviations are used in this manuscript:

RABBIT	Reconstruction of attosecond beating by interference of two-photon transitions
APT	Attosecond pulse train
SFA	Strong-field approximation
TDSE	Time-dependent Schrödinger equation
PES	Photoelectron spectrum
HHn	High n-th order harmonic
NIR	Near infrared
XUV	Extreme ultraviolet
SB	sideband

Appendix A. Attosecond Streaking and Classical Ranges

In Figure 2, the intracycle interference exhibits a 2π-periodic oscillatory pattern as a function of the relative phase ϕ between the fundamental laser and the APT connecting the RABBIT and attosecond streaking methods to infer the phase delays in photoionization. In a dashed line we plot the streaking energy of final HH photoelectron energy as a function of ϕ given by [7]

$$\begin{aligned} E_{\mathrm{str},j}(\phi) &= \left(\sqrt{2((2j+1)\omega - I_P)} + \frac{F_0}{\omega}\sin\phi\right)^2/2 \\ &\simeq (2j+1)\omega - I_P + 2\frac{F_0}{\omega}\sqrt{2((2j+1)\omega - I_P)}\sin\phi. \end{aligned} \tag{A.1}$$

The last line of Eq. (A.1) was obtained by neglecting the $\sin^2\phi$ term for low intensity HH$(2m+1)$. As has been mentioned in Sec. 3, the horizontal bars in Figures 3 and 4 demark the classical energy ranges

 doi:10.20944/preprints202604.1058.v1

for each HH (see Ref. [27]), which are given by the extremes of $E_{\mathrm{str},m}(\phi)$ in Eq. (A.1), that is, when $\sin\phi = 1$ for the upper boundary E_m^+ and $\sin\phi = -1$ for the lower boundary E_m^-, i.e.,

$$E_j^{\pm} = \left(\sqrt{2((2j+1)\omega - I_P)} \pm \frac{F_0}{\omega}\right)^2/2 \tag{A.2}$$

and $j = m, ..., m+\nu-1$ corresponds to the harmonic HH$(2j+1)$ for $m = 13$ and $\nu = 3$ in Figure 3.

References

1. Hentschel, M.; Kienberger, R.; Spielmann, C.; Reider, G.A.; Milosevic, N.; Brabec, T.; Corkum, P.; Heinzmann, U.; Drescher, M.; Krausz, F. Attosecond metrology. *Nature* **2001**, *414*, 509–513. https://doi.org/10.1038/35107000.
2. Paul, P.M.; Toma, E.S.; Breger, P.; Mullot, G.; Augé, F.; Balcou, P.; Muller, H.G.; Agostini, P. Observation of a Train of Attosecond Pulses from High Harmonic Generation. *Science* **2001**, *292*, 1689–1692, [https://science.sciencemag.org/content/292/5522/1689.full.pdf]. https://doi.org/10.1126/science.1059413.
3. Calegari, F.; Sansone, G.; Stagira, S.; Vozzi, C.; Nisoli, M. Advances in attosecond science. *Journal of Physics B: Atomic, Molecular and Optical Physics* **2016**, *49*, 062001. https://doi.org/10.1088/0953-4075/49/6/062001.
4. Huppert, M.; Jordan, I.; Baykusheva, D.; Von Conta, A.; Wörner, H.J. Attosecond Delays in Molecular Photoionization. *Phys. Rev. Lett.* **2016**, *117*, 093001. https://doi.org/10.1103/PhysRevLett.117.093001.
5. He, L.; Sun, S.; Lan, P.; He, Y.; Wang, B.; Wang, P.; Zhu, X.; Li, L.; Cao, W.; Lu, P.; et al. Filming movies of attosecond charge migration in single molecules with high harmonic spectroscopy. *Nature Communications* **2022**, *13*, 4595. https://doi.org/10.1038/s41467-022-32313-0.
6. Itatani, J.; Quéré, F.; Yudin, G.L.; Ivanov, M.Y.; Krausz, F.; Corkum, P.B. Attosecond Streak Camera. *Phys. Rev. Lett.* **2002**, *88*, 173903. https://doi.org/10.1103/PhysRevLett.88.173903.
7. Goulielmakis, E.; Uiberacker, M.; Kienberger, R.; Baltuska, A.; Yakovlev, V.; Scrinzi, A.; Westerwalbesloh, T.; Kleineberg, U.; Heinzmann, U.; Drescher, M.; et al. Direct Measurement of Light Waves. *Science* **2004**, *305*, 1267–1269, [http://science.sciencemag.org/content/305/5688/1267.full.pdf]. https://doi.org/10.1126/science.1100866.
8. Véniard, V.; Taïeb, R.; Maquet, A. Two-Color Multiphoton Ionization of Atoms Using High-Order Harmonic Radiation. *Physical Review Letters* **1995**, *74*, 4161–4164. https://doi.org/10.1103/PhysRevLett.74.4161.
9. Schultze, M.; Fieß, M.; Karpowicz, N.; Gagnon, J.; Korbman, M.; Hofstetter, M.; Neppl, S.; Cavalieri, A.L.; Komninos, Y.; Mercouris, T.; et al. Delay in Photoemission. *Science* **2010**, *328*, 1658. https://doi.org/10.1126/science.1189401.
10. Klünder, K.; Dahlström, J.M.; Gisselbrecht, M.; Fordell, T.; Swoboda, M.; Guénot, D.; Johnsson, P.; Caillat, J.; Mauritsson, J.; Maquet, A.; et al. Publisher's Note: Probing Single-Photon Ionization on the Attosecond Time Scale [Phys. Rev. Lett. 106, 143002 (2011)]. *Phys. Rev. Lett.* **2011**, *106*, 169904. https://doi.org/10.1103/PhysRevLett.106.169904.
11. Guénot, D.; Klünder, K.; Arnold, C.L.; Kroon, D.; Dahlström, J.M.; Miranda, M.; Fordell, T.; Gisselbrecht, M.; Johnsson, P.; Mauritsson, J.; et al. Photoemission-time-delay measurements and calculations close to the 3s-ionization-cross-section minimum in Ar. *Phys. Rev. A* **2012**, *85*, 053424. https://doi.org/10.1103/PhysRevA.85.053424.
12. Feist, J.; Zatsarinny, O.; Nagele, S.; Pazourek, R.; Burgdörfer, J.; Guan, X.; Bartschat, K.; Schneider, B.I. Time delays for attosecond streaking in photoionization of neon. *Phys. Rev. A* **2014**, *89*, 033417, [arXiv:physics.atom-ph/1401.2878]. https://doi.org/10.1103/PhysRevA.89.033417.
13. Pazourek, R.; Nagele, S.; Burgdörfer, J. Attosecond chronoscopy of photoemission. *Reviews of Modern Physics* **2015**, *87*, 765–802. https://doi.org/10.1103/RevModPhys.87.765.
14. Fuchs, J.; Douguet, N.; Donsa, S.; Martin, F.; Burgdörfer, J.; Argenti, L.; Cattaneo, L.; Keller, U. Time delays from one-photon transitions in the continuum. *Optica* **2020**, *7*, 154, [arXiv:physics.atom-ph/1907.03607]. https://doi.org/10.1364/OPTICA.378639.
15. Guénot, D.; Klünder, K.; Arnold, C.L.; Kroon, D.; Dahlström, J.M.; Miranda, M.; Fordell, T.; Gisselbrecht, M.; Johnsson, P.; Mauritsson, J.; et al. Photoemission-time-delay measurements and calculations close to the 3 s-ionization-cross-section minimum in ar. *Physical Review A* **2012**, *85*, 053424. https://doi.org/https://doi.org/10.1103/PhysRevA.85.053424.
16. Boll, D.I.R.; Martini, L.; Fojón, O.A. Analytical model for attosecond time delays and Fano's propensity rules in the continuum. *Phys. Rev. A* **2022**, *106*, 023116. https://doi.org/10.1103/PhysRevA.106.023116.

 doi:10.20944/preprints202604.1058.v1

17. Dahlström, J.M.; Guénot, D.; Klünder, K.; Gisselbrecht, M.; Mauritsson, J.; L'Huillier, A.; Maquet, A.; Taïeb, R. Theory of attosecond delays in laser-assisted photoionization. *Chemical Physics* **2013**, *414*, 53–64. https://doi.org/10.1016/j.chemphys.2012.01.017.
18. Busto, D.; Vinbladh, J.; Zhong, S.; Isinger, M.; Nandi, S.; Maclot, S.; Johnsson, P.; Gisselbrecht, M.; L'Huillier, A.; Lindroth, E.; et al. Fano's propensity rule in angle-resolved attosecond pump-probe photoionization. *Physical review letters* **2019**, *123*, 133201.
19. Isinger, M.; Busto, D.; Mikaelsson, S.; Zhong, S.; Guo, C.; Salières, P.; Arnold, C.; l'Huillier, A.; Gisselbrecht, M. Accuracy and precision of the RABBIT technique. *Philosophical Transactions of the Royal Society A: Mathematical, Physical and Engineering Sciences* **2019**, *377*.
20. Ocello, M.L.; López, S.D.; Barlari, M.; Arbó, D.G. Time-Dependent Theory of Electron Emission Perpendicular to Laser Polarization for Reconstruction of Attosecond Harmonic Beating by Interference of Multiphoton Transitions. *Atoms* **2025**, *13*. https://doi.org/10.3390/atoms13120099.
21. Roantree, L.; van der Hart, H.; Brown, A. Reconstruction of attosecond beating by interference of two-photon transitions with higher-order processes. *Physical Review A* **2025**, *112*, 013118.
22. Reiss, H.R. The tunnelling model of laser-induced ionization and its failure at low frequencies. *J. Phys. B At. Mol. Opt. Phys.* **2014**, *47*, 204006. https://doi.org/10.1088/0953-4075/47/20/204006.
23. Della Picca, R.; Randazzo, J.M.; López, S.D.; Ciappina, M.F.; Arbó, D.G. Laser-assisted photoionization beyond the dipole approximation. *Phys. Rev. A* **2023**, *107*, 053104. https://doi.org/10.1103/PhysRevA.107.053104.
24. Della Picca, R.; Randazzo, J.M.; López, S.D.; Ciappina, M.F.; Arbó, D.G. Nondipole circularly polarized laser-assisted photoelectron emission. *Phys. Rev. A* **2025**, *112*, 023111. https://doi.org/10.1103/hpnr-gwpr.
25. López, S.D.; Donsa, S.; Nagele, S.; Arbó, D.G.; Burgdörfer, J. Phase delays in $\omega - 2\omega$ above-threshold ionization. *Phys. Rev. A* **2021**, *104*, 043113. https://doi.org/10.1103/PhysRevA.104.043113.
26. Arbó, D.G.; López, S.D.; Burgdörfer, J. Semiclassical strong-field theory of phase delays in $\omega - 2\omega$ above-threshold ionization. *Phys. Rev. A* **2022**, *106*, 053101. https://doi.org/10.1103/PhysRevA.106.053101.
27. López, S.D.; Ocello, M.L.; Arbó, D.G. Time-dependent theory of reconstruction of attosecond harmonic beating by interference of multiphoton transitions. *Phys. Rev. A* **2024**, *110*, 013104. https://doi.org/10.1103/PhysRevA.110.013104.
28. Gramajo, A.A.; Della Picca, R.; Garibotti, C.R.; Arbó, D.G. Intra- and intercycle interference of electron emissions in laser-assisted XUV atomic ionization. *Phys. Rev. A* **2016**, *94*, 053404, [arXiv:physics.atom-ph/1605.07457]. https://doi.org/10.1103/PhysRevA.94.053404.
29. Della Picca, R.; Ciappina, M.F.; Lewenstein, M.; Arbó, D.G. Laser-assisted photoionization: Streaking, sideband, and pulse-train cases. *Phys. Rev. A* **2020**, *102*, 043106. https://doi.org/10.1103/PhysRevA.102.043106.
30. Liu, K.; Wang, F.; Liao, Q.; Cao, W.; Lu, P.; Thumm, U. Comprehensive spatial and temporal analysis of attosecond time-resolved photoemission dynamics. *Optics Express* **2026**, *34*, 5102–5118.
31. Bharti, D.; Atri-Schuller, D.; Menning, G.; Hamilton, K.R.; Moshammer, R.; Pfeifer, T.; Douguet, N.; Bartschat, K.; Harth, A. Decomposition of the transition phase in multi-sideband schemes for reconstruction of attosecond beating by interference of two-photon transitions. *Physical Review A* **2021**, *103*, 022834.
32. Bharti, D.; Srinivas, H.; Shobeiry, F.; Bondy, A.; Saha, S.; Hamilton, K.R.; Moshammer, R.; Pfeifer, T.; Bartschat, K.; Harth, A. Multi-sideband interference structures by high-order photon-induced continuum-continuum transitions in helium. *Physical Review A* **2024**, *109*, 023110.
33. Heuser, S.; Jiménez Galán, Á.; Cirelli, C.; Marante, C.; Sabbar, M.; Boge, R.; Lucchini, M.; Gallmann, L.; Ivanov, I.; Kheifets, A.S.; et al. Angular dependence of photoemission time delay in helium. *Physical Review A* **2016**, *94*, 063409.
34. Bertolino, M.; Dahlström, J.M. Multiphoton interaction phase shifts in attosecond science. *Phys. Rev. Res.* **2021**, *3*, 013270. https://doi.org/10.1103/PhysRevResearch.3.013270.